International Journal of Heat and Mass Transfer 70 (2014) 192–201

Contents lists available at ScienceDirect

International Journal of Heat and Mass Transfer

journal homepage: www.elsevier.com/locate/ijhmt

Conjugate heat and mass transfer by jet impingement over a moist protrusion

Maria Valeria De Bonis, Gianpaolo Ruocco *

Scuola d'Ingegneria, Università degli Studi della Basilicata, Campus Macchia Romana, 85100 Potenza, Italy

ARTICLE INFO

Article history:
Received 19 July 2013
Received in revised form 5 November 2013
Accepted 6 November 2013

Keywords:
Mass transfer
Heat transfer
Drying
Jet impingement
Computational fluid dynamics

ABSTRACT

Biosubstrates drying can be intensified, controlled and optimized, even in blunt shapes, by providing exposure to air jet impingement. In this paper round air jet impingement on cylinder protrusions of a model substrate is investigated, for moderate Reynolds numbers and various geometry arrangements.

A comprehensive numerical model, featuring conjugate interface transport (local fluid dynamic effects), multiphase coupling (local surface evaporation) and moisture diffusion notations, is first validated with the corresponding experimental results. Then quantitative distributions of temperature and moisture within the protrusion and along its exposed surface are presented, focussing on the dependence of surface heat and mass transfer on geometry arrangement and fluid dynamic regime. Two values of Reynolds number, two jet heights and two protrusion/jet diameter ratio combinations are investigated.

It is pointed out that, within the investigated range of variables, a protrusion/jet diameter ratio equal to 1 allows for flow patterns that foster process enhancement, but at the expenses of treatment uniformity: after 15 min of treatment the 10% of protrusion only is still relatively moist, but with a strong internal non-uniformity, whereas with a protrusion/jet diameter ratio equal to 3 the untreated part accounts to the 85%, with a smoother internal distribution.

1. Introduction

Most bio-substrate heating is inevitably coupled and intertwined with mass transfer (drying). The most common liquid fraction being water or moisture, evaporation occurs within substrate and at its exposed surface producing vapor which is removed from it. The need of drying is common when seeking substrate stability: by lowering such moisture, handling is promoted and microbial spoilage is prevented, enhancing quality and commercial value. But uncontrolled drying leads to undesired changes in bioactive molecules with their valuable features.

Modeling coupled heat and mass transfer is therefore necessary in these cases, and to ensure approach generality the problem must be attacked simultaneously in both fluid and solid phases. This approach is referred to as the conjugate problem: in this way the heat and mass fluxes vary seamlessly, in space and time, as the solution of field variables. Therefore, no limiting empiricism at phase interface (heat and mass transfer coefficients), usually referring to average conditions and unspecified geometry variations, is introduced.

Jet impingement (JI) has long been recognized for its superior transport characteristics, which can be useful in process intensification, control and optimization. Frequently the involved geometry is more complex than a planar one. Much of the gas JI heat transfer research has been motivated by the need for enhanced cooling of extended surfaces (or blunt corrugations) in limited spaces, as with gas turbine blades or high power CPUs [1]. Reviews on conjugate heat transfer that evidences in a JI configuration can be found in Sarghini and Ruocco [2] (laminar flows) and Yang and Tsai [3] (turbulent flows). Heat transfer was first coupled to mass transfer in conjugate drying due to JI by De Bonis and Ruocco [4] (for a semi-infinite plate) and then by De Bonis and Ruocco [5] and Kurnia et al. [6] (for a flushed substrate): it was evidenced that the drying treatment may be non-uniform, depending on the wall boundary layer that develops locally.

As bio-substrates are often encountered as protrusions, JI can be profitably supplemented to process control and enhancement, and induce a desired superficial finish. In the present framework, a protrusion is a floor or wall-mounted solid with the prevailing length coincident to jet axis. Merci et al. [7] modified the turbulence paradigm to account for the peculiarities of the boundary layer around an impinged blunt cylinder, similar to the geometry speculated in the present paper. Popovac and Hanjalić [8] offered a thorough example of perturbed JI flow and heat transfer around and over a cube protrusion. JI over smooth protrusions have been also studied, as lately by Zhang et al. [9]. Finally, multiple physics effects have even been studied, as the enhancement of heat transfer due to the electromagnetic exposure during JI [10,11]. However, no hints

* Corresponding author. Tel.: +39 0971 205454; fax: +39 0971 205461.
E-mail address: gianpaolo.ruocco@unibas.it (G. Ruocco).

0017-9310/$ - see front matter © 2013 Elsevier Ltd. All rights reserved.
http://dx.doi.org/10.1016/j.ijheatmasstransfer.2013.11.014

Nomenclature

A	pre-exponential factor, 1/s
c	species concentration, mol/m^3
$c_{1\varepsilon}$	model parameter in Eq. (11)
$c_{2\varepsilon}$	model parameter in Eq. (11)
c_{μ}	model parameter in Eqs. (12), (20) and (21)
c^{+}	model parameter in Eq. (21)
c_p	constant pressure specific heat, J/kg K
D	mass diffusivity, m^2/s
E_a	activation energy, J/mol
H	height, thickness, m
k	turbulent kinetic energy, m^2/s^2
K	rate of evaporation, 1/s
L	length, m
M	molecular weight, g/mol
$\mathbf{n}$	normal versor
p	pressure, Pa
Q_{EV}	latent cooling flux, W/m^3
r	radial coordinate, m
R	universal gas constant, J/mol K
Re	Reynolds number
t	time, s
T	temperature, K
U	moisture content, wet basis (kg liquid water/kg substrate)
$\mathbf{v}$	velocity vector, m/s
v	velocity component, m/s
z	vertical coordinate, m

Greek

δ_w	distance from surface, m
δ_w^{+}	dimensionless distance from surface
Δh_{EV}	latent heat of evaporation, J/kg
Δt	process duration, s
ε	turbulent energy dissipation rate, m^2/s^3
κ	Von Kàrmàn's constant
λ	thermal conductivity, W/mK
μ	dynamic viscosity, Pa s
ξ	curvilinear coordinate, m
ρ	density, kg/m^3
σ_k	model parameter in Eq. (11)
σ_{ε}	model parameter in Eq. (11)
ω	air absolute humidity (kg water vapor/kg air)

Superscripts

f	fluid side
s	solid side

Subscripts

0	nominal, initial, reference
a	air
j	jet
l	liquid water
p	plate, process
r	radial component
s	substrate, solid
t	turbulent
v	water vapor
z	vertical component

were found in the available literature concerning coupled heat and mass transfer from a protrusion impinged normally.

The present work is aimed to investigate on JI-enhanced heat and mass transfer from a realistic biomaterial. Initially laminar or moderately turbulent air flows are impinged normally to upright cylinder protrusions. Air velocity, residual moisture and temperature fields can be computed by a conjugate model complemented by a custom evaporation kinetics. Temperature and moisture can be described within the target substrate and along its exposed surface, to speculate on the potential of process finishing and optimization by JI.

2. Analysis

2.1. Flow topology and alteration

A JI configuration over a liquid-saturated protrusion consists in a hot jet flow directed from a round nozzle to the cylindrical target, in a space confined by two parallel plates (Fig. 1). Upon recognition of the nozzle internal geometry, a velocity distribution $v_z(r)$ can be inferred. The configurations at stake in this study consider jet flows that are initially laminar at nozzle, or moderately turbulent. In this case, the impinging flow structure can be summarized into three characteristic regions: the free jet region formed as jet exits, the stagnation (impingement) flow region formed upon jet impact and deflection on protrusion top, and the perturbed boundary layer, along with its recirculation (secondary) pattern, formed upon re-direction of the flow past and along the protrusion. The perturbed boundary layer patterns depend on protrusion height and extension relative to the free jet.

Due to JI, then, large heat and mass transfers are attainable in the vicinity of the stagnation region, but the perturbed boundary layer may contribute to lateral surfaces. At the end, a highly non-uniform drying can result at the exposed surface, with possible local overheating or incomplete evaporation.

2.2. Driving assumptions

Moisture can convert into vapor depending on the heat perturbation front within the substrate. There, liquid moves due to capillarity and solute concentration difference, while vapor moves within the air spaces due to vapor pressure gradients,

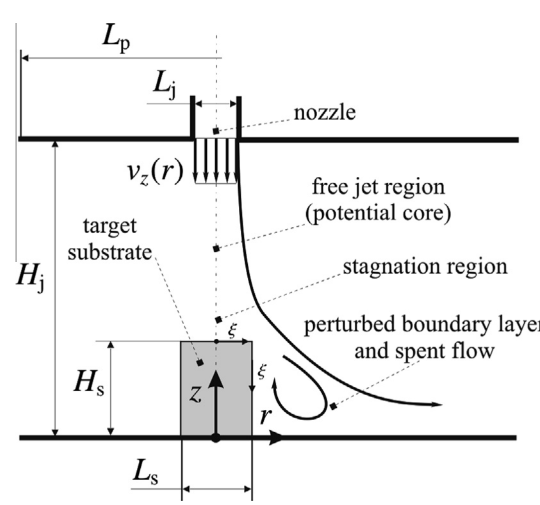

Fig. 1. The adopted geometry and nomenclature, with indication of characteristic flow regions, process coordinates r and z, and curvilinear coordinate ξ.

in both cases assuming Fickian diffusion only [4]. The domain under scrutiny consists in two fluid-and-substrate multi-species sub-domains, sharing the substrate's exposed surface. As transport of liquid is not allowed in the *fluid*, this is a binary system comprising of vapor (v) and drying air (a), while the *substrate* is a ternary system comprising of vapor (v), liquid (l) and solid matter proper (s).

The following additional assumptions are adopted:

1. The flow is axisymmetric and incompressible (negligible pressure work and kinetic energy), with temperature-dependent properties. Due to the adopted flow regime, no body force is accounted for.
2. The substrate is homogeneous and isotropic, with temperature-dependent properties.
3. The viscous heat dissipation is neglected.
4. No-slip is enforced at every solid surface.
5. Due to the nature of the interacting species, no diffusion fluxes are accounted for in the energy equation.
6. The dilute-mixture assumption is appropriate in each sub-domain (the velocity components, temperature and pressure of each species are related to bulk mass in each governing equation).
7. As the turbulence-chemistry interaction is neglected, the evaporation of moisture in the substrate is determined by an Arrhenius expressions (laminar-finite rate model).
8. Neither shrinkage nor deformation of the substrate are accounted for.

2.3. Governing equations

With reference to the previous statements, the standard governing energy, mass and Reynolds-averaged Navier–Stokes equations are enforced [12,13], to yield for temperature, concentrations, velocity components and pressure in both sub-domains. Starting with the energy equation in the substrate:

Transfer of energy, in (s):

$$\rho_s c_{ps}\frac{\partial T_s}{\partial t} = \nabla\cdot(\lambda_s \nabla T_s) - Q_{EV} \tag{1}$$

To attain full energy continuity across the sample's interface or exposed surface, the energy equation in the drying air must be introduced, as well:

Transfer of energy, in (a):

$$\rho_a c_{pa}\frac{\partial T_a}{\partial t} + \rho_a c_{pa}\mathbf{v}\cdot\nabla T_a = \nabla\cdot(\lambda_a\nabla T_a) \tag{2}$$

Q_{EV} in Eq. (1) is the local cooling flux due to the latent heat of evaporation, given by

$$Q_{EV} = M\Delta h_{EV} K c_l \tag{3}$$

where Δh_{EV} is the latent heat of evaporation and K is the rate of evaporation ([13]), with a first-order Arrhenius kinetics:

$$K = A\exp\left(\frac{E_a}{RT_s}\right) \tag{4}$$

The source terms for the transfer of species, associated with this kinetics, must be accordingly included, with the appropriate signs, in the following mass equations:

Transfer of liquid water or moisture, in (s):

$$\frac{\partial c_l}{\partial t} = \nabla\cdot(D\nabla c_l) - Kc_l \tag{5}$$

Transfer of water vapor, in s:

$$\frac{\partial c_v}{\partial t} = \nabla\cdot(D\nabla c_v) + Kc_l \tag{6}$$

To attain full mass continuity across the sample's interface, a mass equation in the drying air must be introduced, as well:

Transfer of water vapor, in (a):

$$\frac{\partial c_v}{\partial t} + \mathbf{v}\cdot\nabla c_v = \nabla\cdot(D\nabla c_v) \tag{7}$$

In order to solve the conjugate problem, Eqs. (2) and (7) are coupled with the following in (a):

Flow continuity:

$$\nabla\cdot\mathbf{v} = 0 \tag{8}$$

Momentum transfer:

$$\rho_a\frac{\partial\mathbf{v}}{\partial t} + \rho_a\mathbf{v}\cdot\nabla\mathbf{v} = -\nabla p + \nabla\cdot(\mu_a+\mu_t)\left[\nabla\mathbf{v} + (\nabla\mathbf{v})^{\mathrm{T}}\right] \tag{9}$$

Transfer of turbulent kinetic energy:

$$\rho_a\frac{\partial k}{\partial t} + \rho_a\mathbf{v}\cdot\nabla k = \nabla\cdot\left[\left(\mu_a + \frac{\mu_t}{\sigma_k}\right)\nabla k\right] + \frac{\mu_t}{2}\left[\nabla\mathbf{v} + (\nabla\mathbf{v})^{\mathrm{T}}\right]^2 - \rho_a\varepsilon \tag{10}$$

Transfer of turbulent energy dissipation rate:

$$\rho_a\frac{\partial\varepsilon}{\partial t} + \rho_a\mathbf{v}\cdot\nabla\varepsilon = \nabla\cdot\left[\left(\mu_a + \frac{\mu_t}{\sigma_\varepsilon}\right)\nabla\varepsilon\right] + \frac{c_{1\varepsilon}\varepsilon\mu_t}{2k}\left[\nabla\mathbf{v} + (\nabla\mathbf{v})^{\mathrm{T}}\right]^2 - \frac{c_{2\varepsilon}\rho_a\varepsilon^2}{k} \tag{11}$$

The present model is based on the standard $k-\varepsilon$ turbulence paradigm [14], having assessed elsewhere its validity [15]. The turbulent viscosity is linked to the model parameter c_μ by the following:

$$\mu_t = \frac{\rho_a c_\mu k^2}{\varepsilon} \tag{12}$$

2.4. Initial and boundary conditions

The absolute humidity-molar concentration conversion is performed according to [13]:

- The *substrate* is initially in thermal equilibrium with the fluid, and saturated with moisture, based on a given initial content, U_0:

$$c_{l0} = 1000\frac{U_0\rho_s}{M}, \quad c_{v0} = 0, \quad T = T_0 \tag{13}$$

- In the quiescent *fluid*, the water vapor content is initially determined by the air absolute humidity, ω, at the given temperature, while no moisture water is present:

$$c_{l0} = 0, \quad c_{v0} = 1000\frac{\omega\rho_a(T_0)}{(\omega+1)M}, \quad v_{r,z} = 0, \quad T = T_0 \tag{14}$$

Furthermore, with reference to Fig. 1, the boundary conditions are as follows:

- Given conditions at jet inlet ($0 \leqslant r \leqslant L_j/2, z = H_j$):

$$c_v = c_{v0}, \quad v_r = 0, \quad v_z = v_z(r), \quad k = k_j, \quad \varepsilon = \varepsilon_j, \quad T = T_j \tag{15}$$

- Symmetry at substrate axis ($r = 0, 0 \leqslant z \leqslant H_s$):

$$\frac{\partial c_{l,v}}{\partial r} = 0, \quad \frac{\partial T}{\partial r} = 0 \tag{16}$$

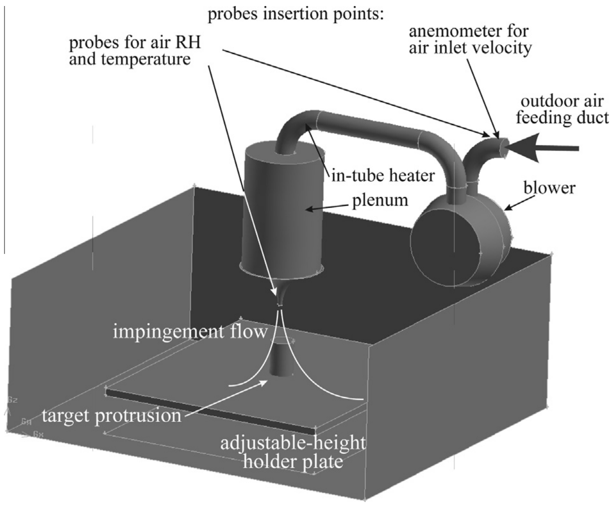

Fig. 2. The test rig. The ceiling and front aperture are removed to show the interiors.

- Symmetry at fluid axis, above the substrate ($r = 0, H_s < z \leqslant H_j$):

$$\frac{\partial c_v}{\partial r} = 0, \quad v_r = 0, \quad \frac{\partial v_z}{\partial r} = 0, \quad \frac{\partial k}{\partial r} = 0, \quad \frac{\partial \varepsilon}{\partial r} = 0, \quad \frac{\partial T}{\partial r} = 0 \tag{17}$$

- At undisturbed distance (outlet) ($r = L_p, 0 < z < H_j$):

$$\frac{\partial c_v}{\partial r} = 0, \quad \frac{\partial v_r}{\partial r} = 0, \quad v_z = 0, \quad \frac{\partial k}{\partial r} = 0, \quad \frac{\partial \varepsilon}{\partial r} = 0, \quad \frac{\partial T}{\partial r} = 0 \tag{18}$$

- No mass flux, given temperature, no-slip and a standard logarithmic wall function for velocity and the turbulence parameters [14], at the upper confinement ($L_j/2 < r \leqslant L_p, z = H_j$) and the lower confinement plates ($0 < r \leqslant L_p, z = 0$):

$$\frac{\partial c_{l,v}}{\partial z} = 0, \text{ substrate interface}, \ \frac{\partial c_v}{\partial z} = 0, \text{ fluid interface}, \ T = T_0 \tag{19}$$

$$\mathbf{n} \cdot \mathbf{v} = 0, \ \mathbf{n} \cdot \nabla k = 0, \ \varepsilon = \frac{c_\mu^{0.75} k^{1.5}}{\kappa \delta_w} \tag{20}$$

$$[(\mu + \mu_t)(\nabla \mathbf{v} + (\nabla \mathbf{v})^T)]\mathbf{n} = \left[\frac{\rho_a c_\mu^{0.25} k^{0.5}}{\ln \delta_w^+ / \kappa + c^+}\right]\mathbf{v}, \ \delta_w^+ = \frac{\delta_w \rho_a c_\mu^{0.25} k^{0.5}}{\mu} \tag{21}$$

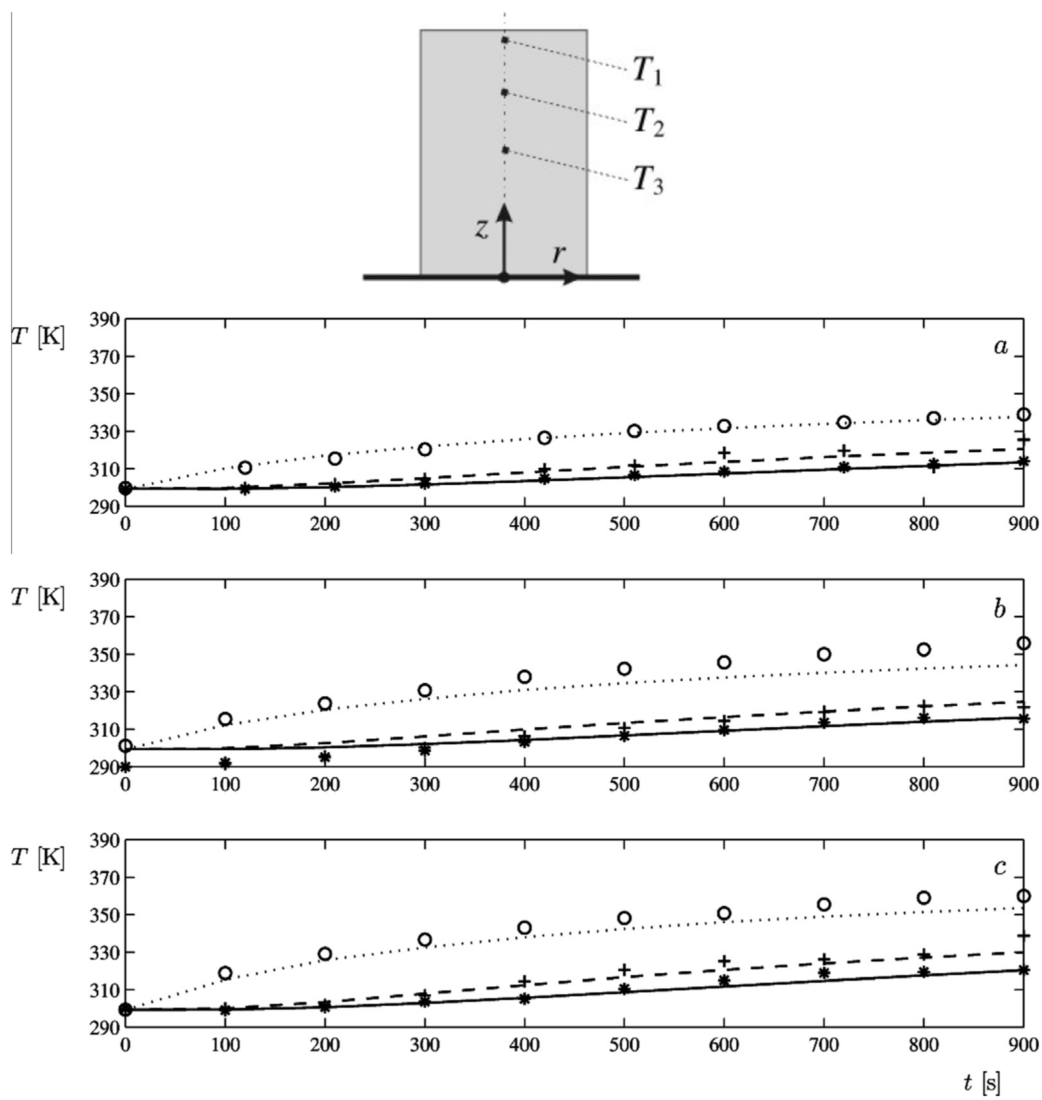

Fig. 3. Thermocouples locations and model validation for $T(t)$, for geometry Case 1, when $v_j = 1.93$ m/s, $T_0 = 299$ K and $\Delta t = 900$ s. Frame a to c: $T_j = 403$, 423 or 453, respectively. T_1: exp. ∘∘∘, num. ⋯; T_2: exp. +++, num. - - -; T_3: exp. ∗∗∗, num. —.

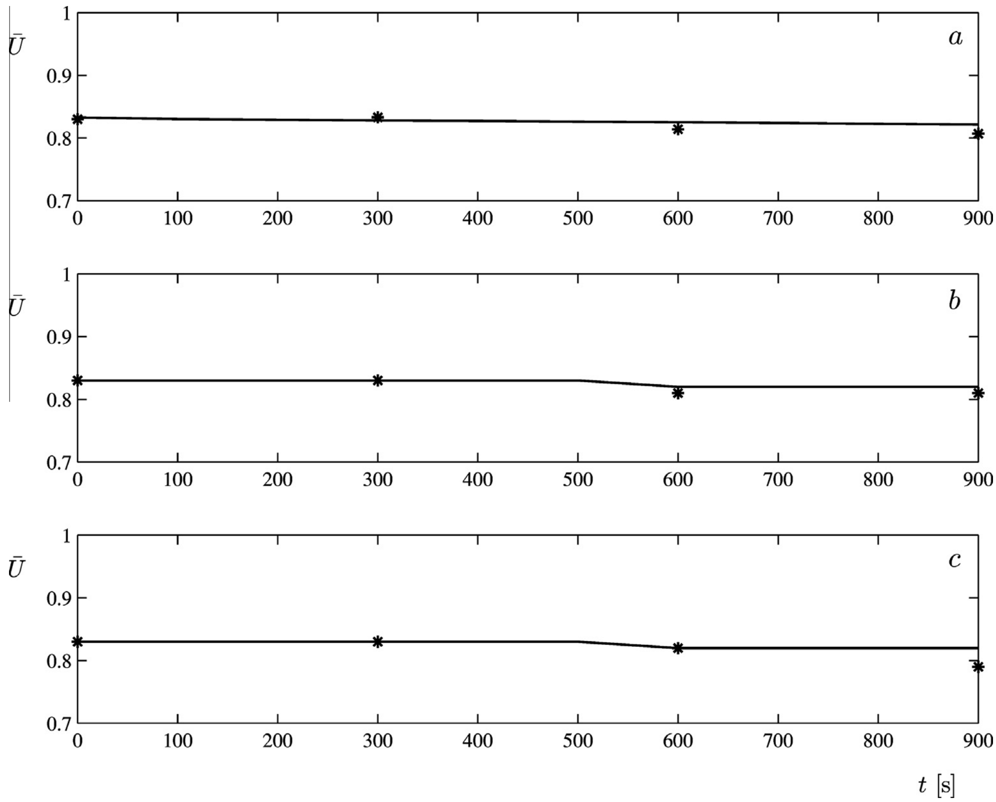

Fig. 4. Model validation for $\bar{U}(t)$, for geometry Case 1, when $v_j = 1.93$ m/s, $T_0 = 299$ K and $\Delta t = 900$ s. Frame *a* to *c*: $T_j = 403$, 423 or 453, respectively. $\bar{U}$: exp. $* * *$, num. —.

Energy and species continuity is allowed, during treatment, to flow through the exposed surface. Therefore, denoting with the superscripts f and s respectively the fluid and the substrate side across such interface:

- Across both the horizontal $(0 \leqslant r \leqslant L_s/2, z = H_s)$ and vertical $(r = L_s/2, 0 \leqslant z \leqslant H_s)$ interfaces:

$$c^f_{l,v} = c^s_{l,v}, \quad T^f = T^s \tag{22}$$

Along this last boundary, Eqs. (20) and (21) also hold.

3. Experiments and model validation

A geometry base-case (Case 1) was first adopted: $H_s = 0.05$ m, $H_j = 0.205$ m, $L_s = 0.03$ m, $L_j = 0.01$ m (Fig. 1). As substrate, fresh (moist) common potatoes were employed, whose properties were taken from Marra et al. [16].

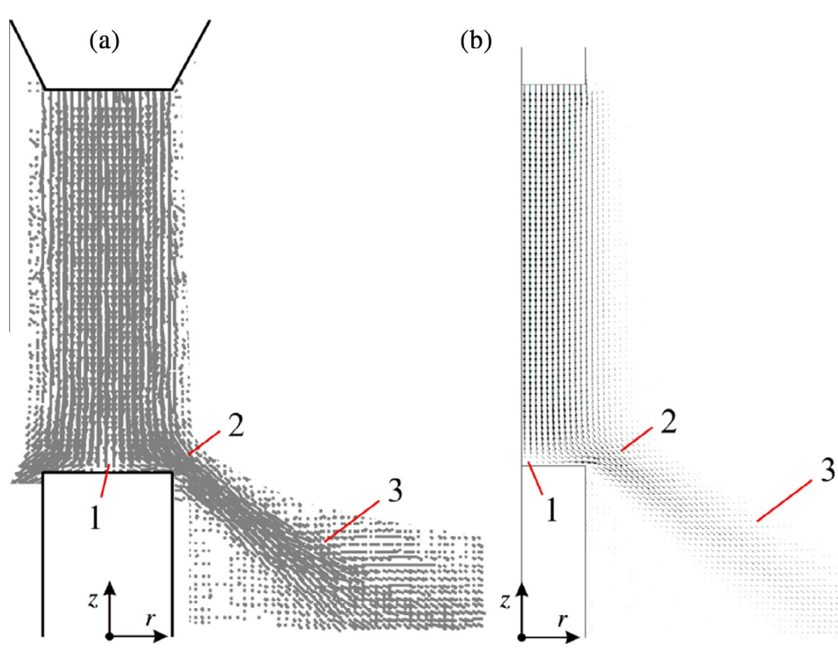

Fig. 5. Qualitative comparison of (a) PIV measurement, and (b) computed flow field, at 3 different loci, for geometry Case 2, with Re_j about 750.

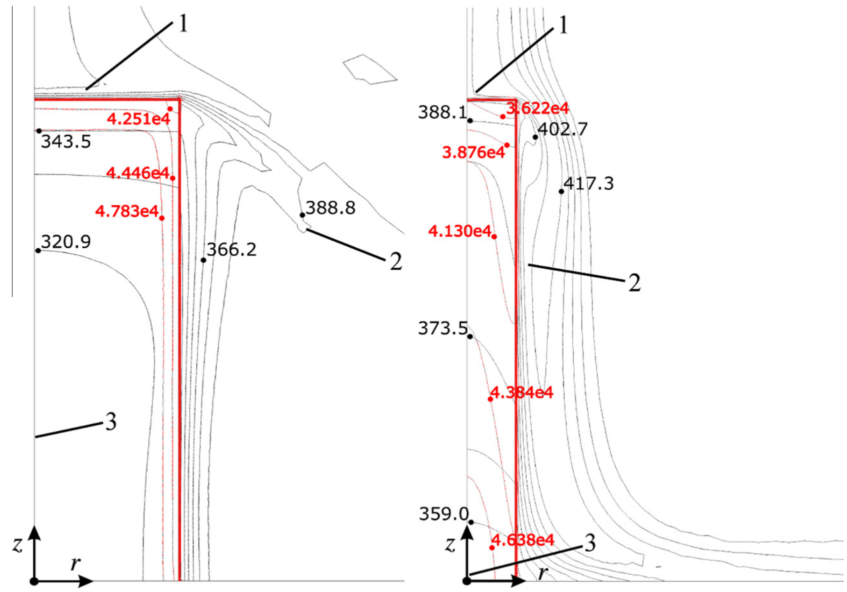

Fig. 6. Contours of T [K] (black) and residual c_l [mol/m^3] (red), with 3 different loci, for $T_j = 423$ K, $T_0 = 299$ K, $Re_j = 750, \Delta t = 900$ s. Left: Case 1; right: Case 2. (For interpretation of the references to colour in this figure caption, the reader is referred to the web version of this article.)

3.1. Numerical treatment

A finite element code has been employed to integrate the system of the governing equations and their initial and boundary conditions. All constants in the turbulence paradigm employed were give their standard values, otherwise those valid for smooth walls [14]. A parallel direct sparse solver is used for the algebraic equation system. A backward differentiation formula of second order is used for the time advancement. The effect of the different values of domain radial length, L_p, has been monitored first, to enforce the boundary condition of undisturbed flow. A value of 20 nozzle diameters was finally chosen along r.

An unstructured meshing technique is used, yielding for triangular element grids. As the process unfolds directly at the exposed substrate surface, the grid-independency test was run by focussing right upon the temperatures over that surface. Several computations were performed by thickening the elements there. Different mesh growth rates and maximum element sides were tried, ranging from 1.3 and $5.0 \cdot 10^{-4}$ m to 1.01 and $1.0 \cdot 10^{-4}$ m, respectively; the selected grid had a combination of 1.05 and $2.5 \cdot 10^{-4}$ m, respectively, yielding for less than 0.1% surface temperature difference with the finer grid. The total number of element was about 9500, in this case.

In order to compare with experimental values for temperature, locally evaluated in discrete volumes due to the size of employed thermocouples (as reported later), the chosen grid was also incremented up to about $11 \cdot 10^3$ elements, to resolve the distortion around their locations.

In any case, execution duration did not exceed a few minutes on a Pentium Xeon server (Linux Ubuntu 12 OS, 3.0 GHz, 16 GB RAM).

The reference rate constant A and the activation energy E_a in Eq. (4) were found as 925 1/s and 48.7 kJ/mol, respectively, based on a multi-object optimization procedure already exploited elsewhere [17].

3.2. Experimental validation

Experiments have been carried out in order to validate the proposed model, for some local temperature and mean residual moisture content, during processing for Case 1. To this end, a laboratory rig was employed (Fig. 2), whose aeraulics was described in De Bonis and Ruocco [5]. The ducting was supplemented with a 10 mm calibrated converging nozzle (TSI, Shoreview, USA). The adoption of a calibrated nozzle was justified by the availability of a precise knowledge on the outlet velocity profile of the jet, which reflects in a uniform $v_z(r) = v_j$ value in Eq. (15) and values as low as 0.005 for both k_j and ε_j in Eq. (15) same.

The auxiliary air is drawn from the environment by a blower and through an electric heater (Leister Process Technologies, Robust and Labo 34, Sarnen, Switzerland) to a relaxation plenum attached to the injection nozzle.

With substrate samples cast as cylindrical chunks, temperature progress was detected in 3 locations (T_1 to T_3) by type-K thermocouples (Labfacility, Dinnington, England), their signals being acquired and converted by a datalogger (Pico Technology, St. Neots, England). The thermocouples were radially inserted up to the axis, directly under the top surface, and at 0.75 and 0.5 cyl-

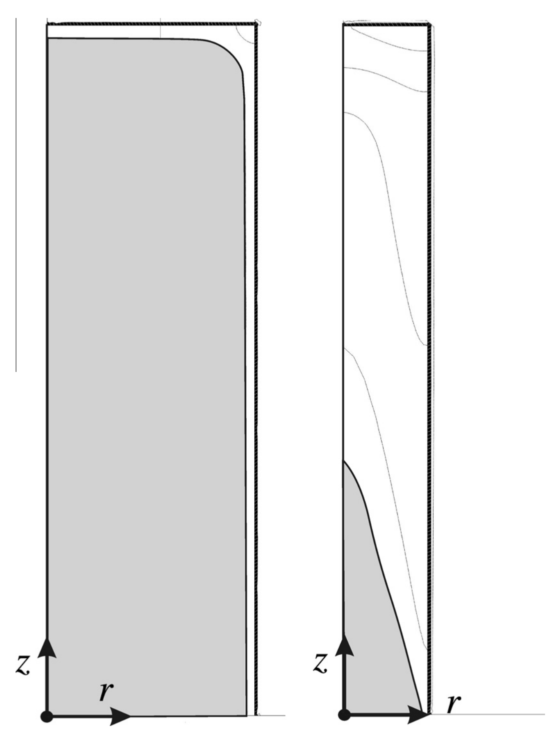

Fig. 7. Protrusion parts which remain with at least the 90% of the initial moisture content, in the same conditions reported in Fig. 6. Left: Case 1; right: Case 2.

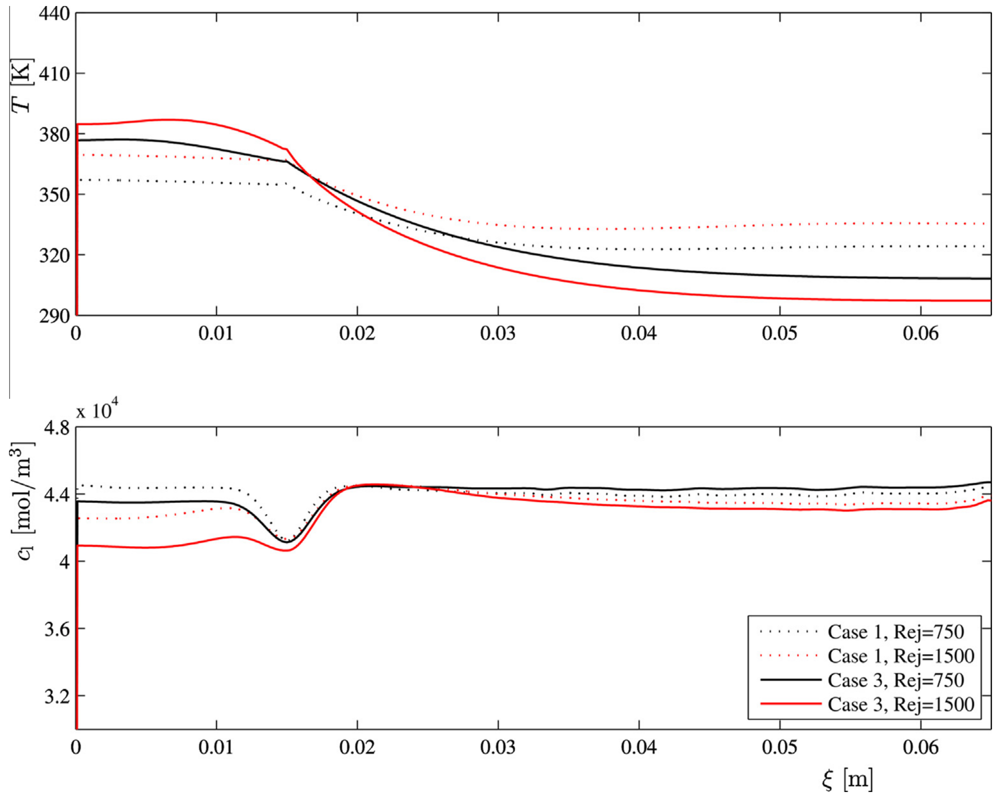

Fig. 8. Profiles of $T(\xi)$ [K] and residual $c_l(\xi)$ [mol/m^3] for $T_j = 423$ K, $T_0 = 299$ K, $\Delta t = 900$ s. Cases 1 and 3, $Re_j = 750$ and 1500.

Table 1
Summary of explored geometry Cases 1 to 4.

Case	H_j [m]	H_s [m]	L_j [m]	L_s[m]
1	0.205	0.05	0.01	0.03
2	0.085	0.05	0.01	0.01
3	0.085	0.05	0.01	0.03
4	0.205	0.05	0.01	0.01

inder heights, respectively (Fig. 3, top). Initially and after 300 s periods, sample drying was evaluated according to AOAC [18] in a convection oven (UFE 400, Memmert, Schwabach, Germany). The initial mean moisture content $\bar{U}_0$ was 0.83. Jet temperature at inlet was varied ($T_j = 403$, 423 or 453 K), with T_0 always about 299 K, while jet velocity at inlet was held constant ($v_j = 1.93$ m/s, yielding an initially laminar jet Reynolds number, $Re_j = \rho_a v_j L_j / \mu_a$, of about 750, which is typical of biosubstrate treatments). Then the model was run to compare with the corresponding experimental results (Figs. 3 and 4), for the same total duration, Δt, of 900 s. In all cases, maximum departures in local temperature and mean moisture values were only few units %.

An uncertainty analysis for residual moisture measurements was performed by following the ISO's Guide to the Expression of Uncertainty in Measurement [19]. For a confidence level of 95%, the mean moisture uncertainty was 0.00566. For the same confidence level, the combined uncertainty due the propagation of uncertainties on the measurement of all other independent variables (velocity, temperature and lengths) was 0.132 in the worst case.

A sample flow field was also qualitatively compared with Particle Image Velocimetry [20]. A new geometry Case 2 was tried for a thinner protrusion under a closer jet, thus varying $L_s = 0.01$ m and $H_j = 0.085$ m only, with Re_j about 750. In Fig. 5 a good agreement between the measurements and the simulated flow field is reported. Indeed, location, shape and extension of significative loci are correspondingly determined: (1) the stagnation region on top of protrusion, (2) the 45°-detached flow past the protrusion edge, and (3) the expansion of the flow in the free field.

4. Results and discussion

4.1. Temperature and residual moisture contours within the protrusion

Contour maps are provided in Fig. 6, for Cases 1 (left) and 2 (right) with the same thermo-fluid dynamics conditions ($T_j = 423$ K, $T_0 = 299$ K, $v_j = 1.93$ m/s, $\Delta t = 900$ s). The initial value for c_l is 4.920×10^4 mol/m^3. It is first seen for Case 1 (Fig. 6, left) that: (1) the isotherms are densely packed on protrusion top, as expected, with a wide stagnation region spanning half a cylinder radius, (2) the deflected jet carries some heat past the corner, away as a spent flow in the perturbed boundary layer (Fig. 1), and (3) as the exposure is highly non-symmetrical, a slowest heating zone is found moved towards the bottom. Then the iso-moisture lines are seen to follow regularly the exposed surface, which dries uniformly throughout but more effectively at top as expected, with the exception of a some enhancement at corner.

Then let us turn on Case 2 (Fig. 6, right): (1) under a more direct jet flow and for a smaller target, the stagnation region is barely seen, (2) the flow jet indeed runs over the protrusion and reattaches at the vertical side, forming a wall boundary layer, eventually impacting on the floor, and (3) the slowest heating point is found definitely near the protrusion bottom. Due to the more effective thermo-fluid dynamics driving forces, now found even on protrusion lateral side, a stronger drying is seen favoring non-uniform internal treatment, in the same conditions.

Fig. 7 illustrates this concept, helping quantify the treatment extent. It is seen at left, for the same Case 1 reported earlier in Fig. 6, that the part remaining fresh (high water content) i.e. with at least the 90% of the initial moisture is rather large, accounting to about

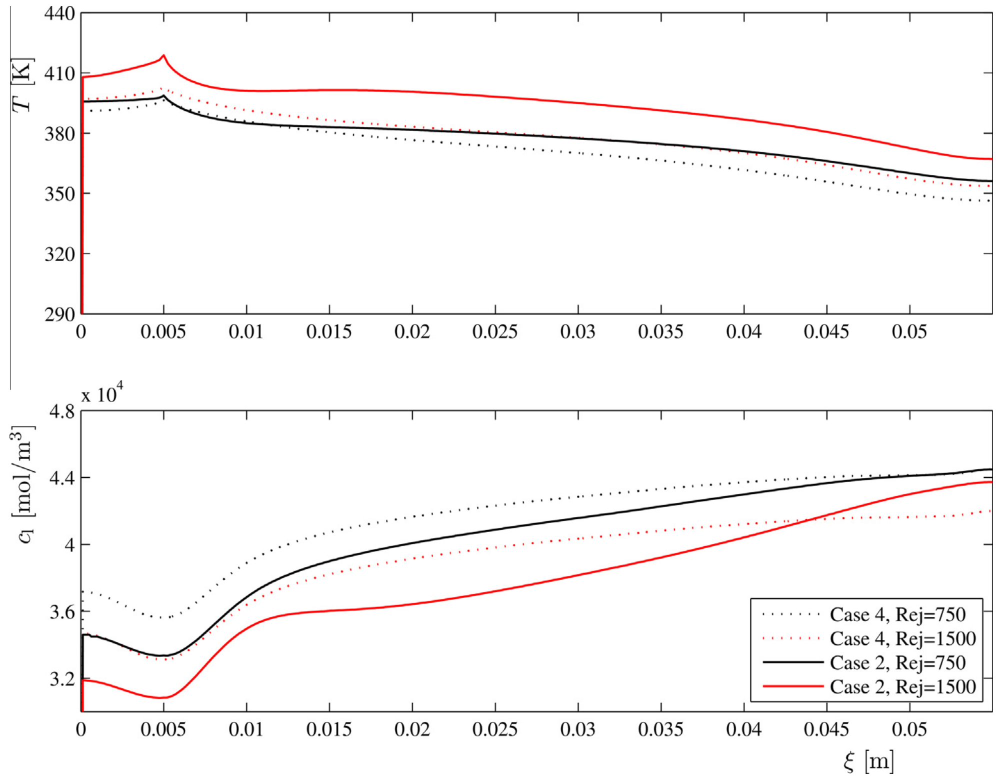

Fig. 9. Profiles of $T(\xi)$ [K] and residual $c_l(\xi)$ [mol/m^3] for $T_j = 423$ K, $T_0 = 299$ K, $\Delta t = 900$ s. Cases 2 and 4, $Re_j = 750$ and 1500.

85% of total volume. Conversely, in Fig. 7, right, under the same circumstances, this part (90% of the initial moisture) accounts to about 10% of total volume only, for the more severe Case 2.

4.2. Temperature and moisture profiles on the exposed surface

As implied earlier, JI can be employed to induce a desired superficial finish. The coupled mechanisms of heat and mass transfer, as altered in turn by interfacial momentum transfer, are such that their effect on the finish varies in unexpected ways. Now, a curvilinear coordinate ξ that follows the exposed cylinder side (Fig. 1) is employed to report on the local temperature and residual moisture at interface: from symmetry boundary ($\xi = 0$ for $r = 0, z = H_s$) to lower confinement plate ($\xi = L_s/2 + H_s$ for $r = L_s/2, z = 0$). T_j and T_0 are kept to 423 and 299 K, respectively. Geometry Cases 1 and 2 will be now combined, generating two more Cases.

Let us start with $T = T(\xi)$ after $\Delta t = 900$ s in Fig. 8, top, for two jet velocities or flow rates ($Re_j = 750$ or 1500) and the two jet heights ($H_j = 0.205$ or 0.085 m), while keeping the protrusion size $L_s = 0.03$ m (Cases 1 and 3, respectively, see Table 1). Maximum temperature is found away from symmetry, as common in JI, but only for the closer jet discharge configuration (Case 3): the protrusion is heated up by some 20 K on the top region with respect to the farthest jet configuration (Case 1), while doubling the flow rate increments temperature to 12 K at most. It is interesting to note that closer discharge (Case 3) induces poorer and non-uniform lateral heating. This effect is most evident for the higher flow rate, due to the aforementioned lateral flow patterns: the temperature profile is therefore inverted starting slightly past the protrusion corner ($\xi = 0.17$ m) for $Re_j = 1500$, while it occurs later ($\xi = 0.27$ m) in the alternate case. It is also instructive to inspect in Fig. 8, bottom, the local moisture concentration $c_l = c_l(\xi)$. The surface drying follows closely the temperature profile in the given conditions, with a negative inflection at the corner, slightly stronger for Case 3 and $Re_j = 1500$. Along the lateral side, drying appears rather smooth in any case.

Then a smaller protrusion is inspected ($L_s = 0.01$ m) in Fig. 9, top (Cases 2 and 4, see Table 1). $T = T(\xi)$ shows a positive inflection point at corner, which is stronger for the closer and larger jet flow (Case 2 and $Re_j = 1500$), but gets inverted in no case. In the most effective configuration, T is always higher, by a maximum 17 K. Stronger heating enhances drying but non-uniformities exist along the entire protrusion profile, in Fig. 9, bottom: but concentration differences never exceed 5000 mol/m^3, which is mere 10% of the initial moisture value. In the most effective configuration, the protrusion corner is more dried by almost the 23% with respect to part that lies on the floor. Cross-inspection of Figs. 8 and 9 indeed reveals that the most effective parameter is the L_s/L_j ratio: between the two explored values 1 and 3 (Fig. 9 versus Fig. 8, respectively), the former favors overall drying enhancement (up to 25%) but with a uniformity payoff on the protrusion lateral side.

Finally, in the last Fig. 10 the influence of flow patterns on surface finish is reported, for Cases 2 (top) and 3 (bottom). Two main features of flow are emphasized by proper labeling: acceleration past the protrusion corner, and subsequent pattern. It can be seen that the wall boundary layer for Case 2 (Fig. 10, top), already alluded to when discussing Fig. 6 (right), must be held responsible for the strong non-uniformity detected along the exposed surface and, by combining the species diffusion and phase change, for the spatial gradient in the residual moisture distribution within the substrate self. Conversely, for a thicker protrusion under the same conditions (Case 3 in Fig. 10, bottom), the flow pattern is such that the warm fluid cannot run over and along the lateral side of protrusion, being detached in the free field past the corner (forming only a mild recirculation field along the protrusion), therefore resulting ineffective in removing moisture.

4.3. Comparison with the available literature

In the search for available comparisons, the flow field data by Merci et al. [7] were first scrutinized. Their geometry was fairly

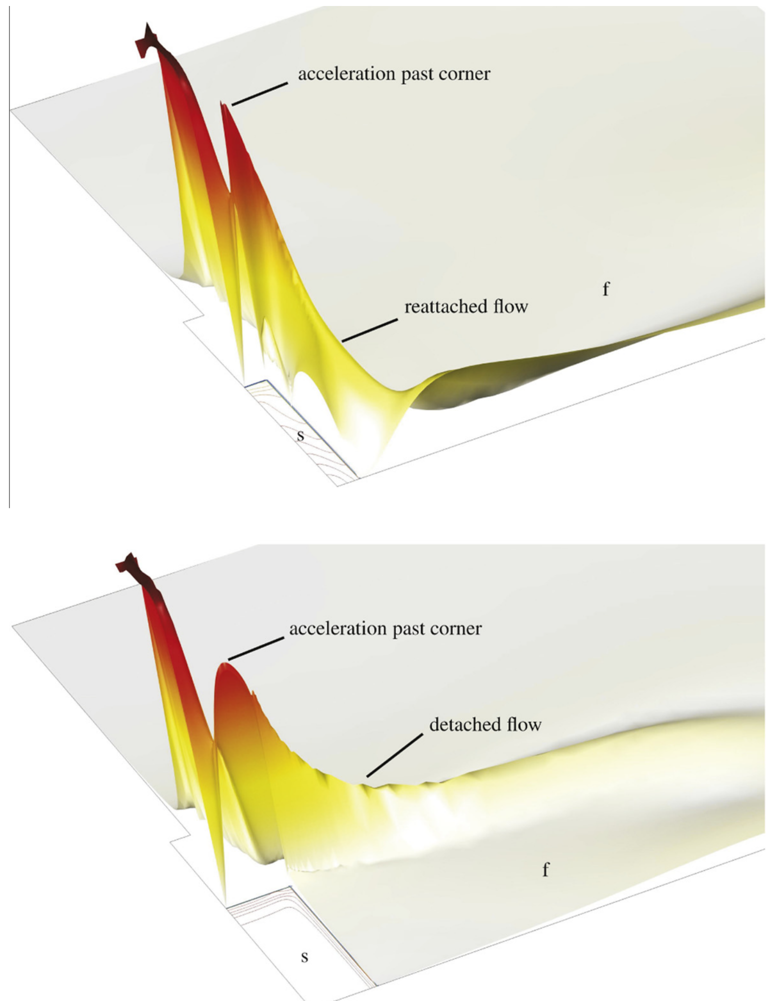

Fig. 10. Qualitative 3D representation of $|\mathbf{v}|$ (in the fluid f), with contours of residual c_l (in the solid s), for Case 2 (top) and Case 3 (bottom), for $T_j = 423$ K, $T_0 = 299$ K, $Re_j = 1500$ and $\Delta t = 900$ s.

close to the present Case 1, but the flow field is fully turbulent ($Re_j = 23000$ and counting), which is inadequate for biosubstrate treatments. Similarly, heat transfer data were reported by Zhang et al. [9], for the milder flow situation ($Re_j = 5000$), but again their smooth geometry did not perturbed the flow but with a weak detachment, differently than with the present topology (see discussion of Figs. 5 and 10), and consequently the surface temperature cannot be compared with the one at stake here. The study performed by Popovac and Hanjalic [8], typical of electronic cooling systems, brought over some similarities with the present Case 3, but the flow field strength was again in excess with respect to the milder situation reported in the present paper. Their 3D simulation, although perturbed by a bulk cross flow, showed how the complex vortex and wake morphology does influence the local heat transfer, bringing forth temperature non-uniformities along exposed surfaces and edges, similarly with the effects reported qualitatively in Fig. 10, and quantitatively in Fig. 8 more than 80 K difference along the exposed surface, for Case 3 with $Re_j = 1500$.

5. Conclusions

An axisymmetric transfer phenomena model is developed to study the transient behavior of temperature and moisture content within a moist protrusion, under an air impinging jet. The drying performance of the process is analyzed with the effect of air flow distribution and temperature. The model features a generalized approach based on a conjugate treatment of heat and mass exchange, with no resort to interface empiricisms, and a custom kinetics for water evaporation.

Such an approach allowed for the assessment of the influence of the main driving parameters (jet height and flow rate, and protrusion size) on thermal and moisture concentration distributions within the sample and along its exposed surface.

The validation has been brought forth against the associated experimental data reporting on local temperature and mean residual moisture for a model biosubstrate. As a good agreement was reached, the model was exercised for 4 geometry and operating cases among which the most severe was found, for the small protrusion under close jet discharge, which led to strong non-uniform moisture content and surface finish.

References

[1] N. Zuckerman, N. Lior, Jet impingement heat transfer: physics, correlations, and numerical modeling, in: G.A. Greene, J.P. Hartnett, A. Bar-Cohen, Y.I. Cho (Eds.), Advances in Heat Transfer, Academic Press, New York, 2006, pp. 565–631.
[2] F. Sarghini, G. Ruocco, Enhancement and reversal heat transfer by competing modes in jet impingement, Int. J. Heat Mass Transfer 47 (2004) 1711–1718.
[3] Y.-T. Yang, S.-Y. Tsai, Numerical study of transient conjugate heat transfer of a turbulent impinging jet, Int. J. Heat Mass Transfer 50 (2007) 799–807.

[4] M.V. De Bonis, G. Ruocco, Modelling local heat and mass transfer in food slabs due to air jet impingement, J. Food Eng. 78 (2007) 230–237.
[5] M.V. De Bonis, G. Ruocco, An experimental study of the local evolution of moist substrates under jet impingement drying, Int. J. Therm. Sci. 50 (2011) 81–87.
[6] J.C. Kurnia, A.P. Sasmito, W. Tong, A.S. Mujumdar, Energy-efficient thermal drying using impinging-jets with time-varying heat input – a computational study, J. Food Eng. 114 (2013) 269–277.
[7] B. Merci, M.P.E. Mesbah, J.W. Baughn, Experimental and numerical study of turbulent heat transfer on a cylindrical pedestal, Int. J. Heat Fluid Flow 26 (2005) 233–243.
[8] M. Popovac, K. Hanjalić, Vortices and heat flux around a wall-mounted cube cooled simultaneously by a jet and a crossflow, Int. J. Heat Mass Transfer 52 (2009) 4047–4062.
[9] D. Zhang, H. Qu, J. Lan, J. Chen, Y. Xie, Flow and heat transfer characteristics of single jet impinging on protrusioned surface, Int. J. Heat Mass Transfer 58 (2013) 18–28.
[10] S. Geedipalli, A.K. Datta, V. Rakesh, Heat transfer in a combination microwave-jet impingement oven, Food Bioprod. Process. 86 (2008) 53–63.
[11] M. Pace, M.V. De Bonis, F. Marra, G. Ruocco, Characterization of a combination oven prototype: effects of microwave exposure and enhanced convection to local temperature rise in a moist substrate, Int. Commun. Heat Mass Transfer 38 (2011) 557–564.
[12] R.B. Bird, W.E. Stewart, E.N. Lightfoot, Transport Phenomena, John Wiley & Sons, New York, 1995.
[13] M.V. De Bonis, G. Ruocco, A generalized conjugate model for forced convection drying based on an evaporative kinetics, J. Food Eng. 89 (2008) 232–240.
[14] D.C. Wilcox, Turbulence Modeling for CFD, DCW Industries, La Cañada, 1998.
[15] M. Angioletti, E. Nino, G. Ruocco, CFD turbulent modelling of jet impingement and its validation by particle image velocimetry and mass transfer measurements, Int. J. Therm. Sci. 44 (2005) 349–356.
[16] F. Marra, M.V. De Bonis, G. Ruocco, Combined microwaves and convection heating: a conjugate approach, J. Food Eng. 97 (2010) 31–39.
[17] M.V. De Bonis, G. Ruocco, Computational transport phenomena in bioprocessing with the approach of the optimized source term in the governing equations, Heat Mass Transfer 48 (2012) 1485–1493.
[18] AOAC, Official Methods of Analysis, 16th ed., Association of Official Analytical Chemists, Gaithersburg, 1995, Method 925.10.
[19] P.F. Dunn, Measurements and Data Analysis for Engineering and Science, McGraw-Hill, New York, 2005. pp. 263–282.
[20] M. Angioletti, R.M. Di Tommaso, E. Nino, G. Ruocco, Extended visualization by particle image velocimetry of impinging jets on a protrusion, and comparison with simulations, in: E. Nino, G. Ruocco (Eds.), Proceedings of the Twentieth UIT National Heat Transfer Conference, Edizioni ETS, Pisa, Italy, 2002, pp. 163–168.